ARTICLES
https://doi.org/10.1038/s41560-019-0464-5
nature energy

Monolithic solid–electrolyte interphases formed in fluorinated orthoformate-based electrolytes minimize Li depletion and pulverization

Xia Cao[1], Xiaodi Ren[1], Lianfeng Zou[2], Mark H. Engelhard[2], William Huang[3], Hansen Wang[3], Bethany E. Matthews[2], Hongkyung Lee[1], Chaojiang Niu[1], Bruce W. Arey[2], Yi Cui[3], Chongmin Wang[2], Jie Xiao[1], Jun Liu[1], Wu Xu[1]* and Ji-Guang Zhang[1]*

Lithium (Li) pulverization and associated large volume expansion during cycling is one of the most critical barriers for the safe operation of Li-metal batteries. Here, we report an approach to minimize the Li pulverization using an electrolyte based on a fluorinated orthoformate solvent. The solid–electrolyte interphase (SEI) formed in this electrolyte clearly exhibits a monolithic feature, which is in sharp contrast with the widely reported mosaic- or multilayer-type SEIs that are not homogeneous and could lead to uneven Li stripping/plating and fast Li and electrolyte depletion over cycling. The highly homogeneous and amorphous SEI not only prevents dendritic Li formation, but also minimizes Li loss and volumetric expansion. Furthermore, this new electrolyte strongly suppresses the phase transformation of the $LiNi_{0.8}Co_{0.1}Mn_{0.1}O_2$ cathode (from layered structure to rock salt) and stabilizes its structure. Tests of high-voltage Li||NMC811 cells show long-term cycling stability and high rate capability, as well as reduced safety concerns.

The ever-increasing demand for high-energy-density batteries has revitalized worldwide efforts on rechargeable lithium (Li) metal batteries (LMBs) in recent years. However, significant challenges relating to the stability of the Li-metal anode (LMA) still limit the large-scale application of LMBs[1–8]. The thermodynamic instability of metallic Li can lead to continuous side reactions between Li and electrolyte, and continuous loss of Li metal and electrolyte, yielding low Li Coulombic efficiency and short cycle life[2,6]. Even in the case of Li growth with high Coulombic efficiency and without dendrites, pulverization of LMA and its large volumetric expansion after long-term cycling still entail great safety concerns, especially for the nail-penetration test after cycling[6,9].

Since Li nucleation and growth are predominantly determined by the chemical nature of the electrolytes, developing electrolytes that have good stability with Li, which forms a uniform, robust solid–electrode interphase (SEI) on the LMA, is critical and urgently needed for further development of LMBs[10–16]. Because metallic Li is thermodynamically unstable with almost all organic solvents[17], SEI formed on LMA plays a key role in its stable cycling[18]. Two types of SEI structure (that is, mosaic type (composed of randomly distributed inorganic parts (sometimes crystals) and organic parts (polymers)) and multilayer type (composed of an inner inorganic layer and an outer organic layer)) have been observed and widely accepted in the field[18–21]. However, these SEI layers continuously grow during the repeated charge/discharge processes, leading to fast Li and electrolyte depletion over cycling. Therefore, further improvements on the SEI composition and structure, with great uniformity and robustness against cycling, are critical for the stable operation of LMAs.

The stability of electrolyte with cathodes is also important. Some electrolytes that exhibit excellent stability with LMA may not be stable with high-voltage cathodes, such as $LiNi_{0.8}Co_{0.1}Mn_{0.1}O_2$ (NMC811)[22]. Therefore, an ideal electrolyte needs to form a stable cathode–electrolyte interphase (CEI) on the cathode to enable high-energy-density batteries[5,23]. Although many common solvents used in Li-ion batteries, such as carbonates, sulfones, phosphates, nitriles and ionic liquids, are oxidatively stable up to 4.5 or even 5 V (versus Li/Li^+), their applications in LMBs are limited due to their poor stability against metallic Li[1,11,15,24,25]. Among the reported electrolyte solvents, ethers are always appealing for LMAs because their high reductive stability with Li leads to much higher Coulombic efficiency and less dendritic Li than the carbonate solvents typically used in Li-ion batteries[26]. However, ether-based electrolytes have limited applications in practical batteries because of their low anodic stability, which is normally <4 V when used with a nominal salt concentration (~1 M). An interesting approach is using fluorinated solvents[23,27,28]. Unlike the mainstream nonfluorinated solvents (including regular ethers, esters, carbonates, phosphates, sulfones and nitriles) that have either good anodic stability or Li stability, fluorinated solvents (including fluorinated ethers, carbonates and sulfones) can shift the oxidation stability to a higher voltage, and at the same time more readily stabilize the Li anode to a certain extent, by forming a robust LiF-rich SEI[11,14,23,29–36]. Nevertheless, continuous side reactions and fast Li depletion still occur.

In recent years, superconcentrated electrolytes (or high-concentration electrolytes (HCEs)) were proposed to stabilize both the high-voltage cathode and the LMA by reducing the number of free solvent molecules and modifying the Li^+ solvation structure[5,35,37–39]. However, most HCEs exhibit high viscosity, which is not good for wetting electrodes and separators in practical applications[11,36]. More recently, localized HCEs have been developed using various diluents in the HCEs to minimize the above disadvantages of HCEs[11,12,33–36,40].

[1]Energy and Environment Directorate, Pacific Northwest National Laboratory, Richland, WA, USA. [2]Environmental Molecular Sciences Laboratory, Pacific Northwest National Laboratory, Richland, WA, USA. [3]Department of Materials Science and Engineering, Stanford University, Stanford, CA, USA. *e-mail: wu.xu@pnnl.gov; jiguang.zhang@pnnl.gov

Table 1 | Physical properties of TFEO and conventional solvents

Compound	DFT calculation		Boiling point (°C)	Viscosity at 30 °C (cP)
	HOMO (eV)	LUMO (eV)		
EC 	−8.47	−0.28	243	1.90 (at 40 °C)[24]
EMC 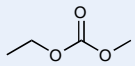	−8.14	−0.07	107	0.65[24]
DME 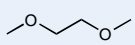	−7.19	−0.18	85	0.46[24]
TFEO 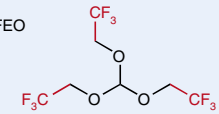	−9.06	−0.63	143	0.43

LUMO, lowest unoccupied molecular orbital.

Although these approaches have largely improved the stability of LMA and extended the cycle life of LMBs[3], significant increases in the cell thickness and pulverization of LMA are still observed after long-term cycling.

In this work, we propose a class of fluorinated solvents—hydrofluoro-orthoformates—to minimize Li depletion and pulverization in LMBs. For instance, tris(2,2,2-trifluoroethyl)orthoformate (TFEO) (see Table 1 for its structure) exhibits a high boiling point of 145 °C, which may enable battery application at elevated temperatures, and can largely improve the stability and safety of LMBs. Moreover, TFEO does not contain any unstable functional groups (such as cyano, carbonyl and sulfonic groups) that are highly reactive with metallic Li, but only contains Li-friendly ether groups that ensure its stability against Li[16]. TFEO also possesses a powerful electron-withdrawing group (CF_3), which extends its oxidative stability[41–43]. It exhibits a very low highest occupied molecular orbital (HOMO) energy value compared with other typical solvents, as shown in Table 1. This property largely enhances its high-voltage stability. At the same time, its low viscosity makes it an excellent electrolyte co-solvent (or diluent). Specifically, 1 M LiFSI in DME-TFEO (1:9 by weight and 1.2:3 by mole; hereafter referred to as 1 M LiFSI/DME-TFEO) was used in this work. One of the distinguished advantages of TFEO-based electrolytes is that they can form a monolithic SEI, whose highly homogeneous and inorganic rich properties largely minimize the pulverization of LMA even after long-term cycling, which is critical for the safe operation of LMBs.

Monolithic SEI on Li anode

Figure 1a–c shows high-resolution cryo-electron microscopy (cryo-EM) images of the Li-metal particles formed after the first electrochemical deposition in the TFEO-based electrolyte. In general, continuous and uniform SEI is found on the surface of the deposited Li, as shown Fig. 1a,b. When cryo-EM magnification is further increased to an atomic scale, the Li growth direction and SEI structure become visible. The dashed lines in Fig. 1c show a consistent SEI thickness of ~10 nm on the Li surface. In parallel, the energy dispersive spectroscopy spectrum inserted in Fig. 1c proves that this SEI is rich in inorganic species (that is, there are much higher levels of O-, F- and S-containing compounds derived from LiFSI than C-containing organic species). Interestingly, these inorganic compounds in this SEI layer were not crystallized. Instead, they were distributed uniformly in an amorphous state in this particular SEI, as shown by the corresponding selected-area electron diffraction inserted in Fig. 1a and reduced fast Fourier transform result shown in Fig. 1c, where only the crystalline Li structure is identified. This SEI structure is completely different from those reported in the literature[18,19,24]. For the well-known mosaic- and multilayer-type SEI structures, the inorganic species were usually crystallized and enriched in certain areas of the SEI[18,19,24], thus these SEIs were not as homogenous as would be expected for an ideal SEI. However, the SEI formed in this TFEO-based electrolyte exhibited a fully amorphous structure, although it was also rich in inorganic species. Moreover, this SEI proved to be uniform not only in horizontal coverage, but also in depth through the SEI from the surface to the bottom (close to the Li metal), as discussed in detail below. A schematic of the observed SEI on the Li is shown in Fig. 1d.

Extended cycling and minimized Li depletion/pulverization

Electrochemical performance characterizations and post-cycling analysis further validated the unique SEI properties generated in TFEO-based electrolyte. In this work, conventional carbonate electrolyte (1 M $LiPF_6$/ethylene carbonate (EC)-ethyl methyl carbonate (EMC) + 2% vinylene carbonate (VC) and ether-based electrolyte (1 M LiFSI/1,2-dimethoxyethane (DME)) were used as reference electrolytes. The physical properties of these electrolytes, such as conductivity, viscosity and wettability, are shown in Supplementary Fig. 1a,b. Fig. 2a shows the electrochemical stability window of the three electrolytes. The carbonate-based electrolyte shows slight oxidation starting at 4.2 V. For the 1 M LiFSI/DME electrolyte, the oxidation begins at slightly higher than 3.5 V due to the low anodic stability of DME. However, for the 1 M LiFSI/DME-TFEO electrolyte, oxidative stability of the electrolyte improves dramatically, and no noticeable oxidative current is observed until 6 V.

Figure 2b shows the voltage profiles from evaluation of the Li Coulombic efficiencies of the electrolytes. 1 M LiFSI/DME showed an Li Coulombic efficiency of 98.1%, which was much higher than that of the reference electrolyte (89.8%). With the addition of TFEO, the 1 M LiFSI/DME-TFEO showed an excellent Li Coulombic efficiency of 99.5%, which is one of the best values reported for LMAs. The first-cycle voltage profiles of these electrolytes are presented in Supplementary Fig. 2. These different Coulombic efficiency values are consistent with the Li deposition morphologies shown in Supplementary Fig. 3a–c. Large and more compact granular Li particles were deposited on the Cu substrate in 1 M LiFSI/DME-TFEO, while dendritic Li formed in the reference carbonate electrolyte and less compact Li was deposited in 1 M LiFSI/DME, probably because of the highly uniform SEI formed in this electrolyte.

Figure 2c shows the cycling performance of the symmetrical Li||Li cells. The voltage curve of the cell using the reference electrolyte showed a rapid increase in polarization after 300 h, and the cell failed at ~450 h. In contrast, the cells using 1 M LiFSI/DME and 1 M LiFSI/DME-TFEO electrolytes showed very stable cycling for more than 700 h. Supplementary Fig. 4b,c shows magnified views of the first 20 h and the 20 h after 400 h, respectively. Figure 2d shows the cycling performance of the Li||NMC811 cells. The voltage profiles for these cells are shown in Supplementary Fig. 5a–c. The cell with the reference carbonate electrolyte showed stable cycling in the first 30 cycles and then a sudden drop in both capacity and Coulombic efficiency, which can be attributed to rapid consumption of Li. The shorter cycle life compared with the literature report for reference electrolyte is because of the very thin Li anode (50 µm) used in this work compared with previous reports[14,28,44]. Supplementary Fig. 6 shows that the Li||NMC811 cells with a thicker Li anode (450 versus 50 µm) exhibit a much longer cycle life, but a much thinner Li anode is required to realize the full potential of LMBs. For the cell with 1 M LiFSI/DME, the cell capacity decreased slowly in the first 25 cycles, decayed somewhat quickly in the 25th–50th cycles, and then dropped abruptly, with an extended cycle number of ~50 cycles before the cell failed. For this cell, the capacity decay and low Coulombic efficiency during the cycling can be partially attributed

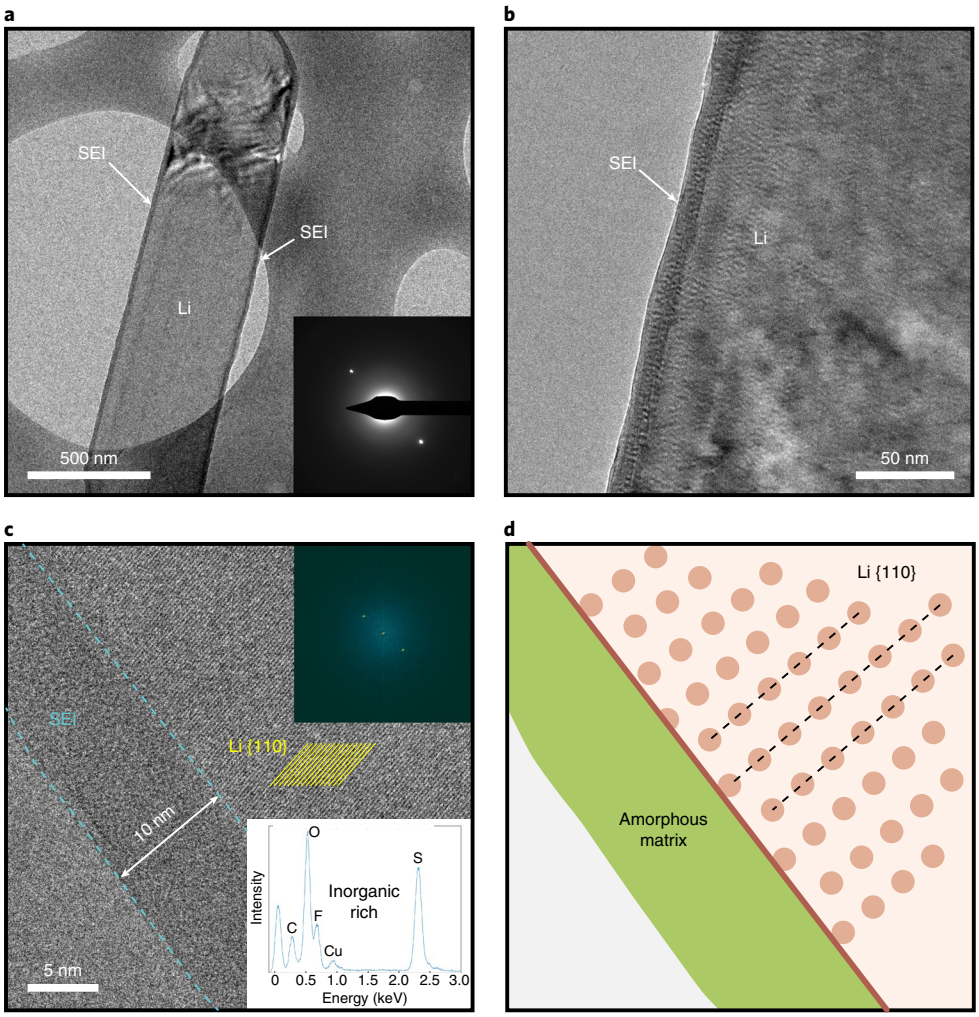

Fig. 1 | SEI on the Li anode. a–**c**, Cryo-EM images of Li deposited on a TEM grid at different scales. Inset in **a**: corresponding selected-area electron diffraction pattern. Inset in **c**: corresponding reduced fast Fourier transform (top) and energy dispersive spectroscopy spectra (bottom) of the SEI layer. The yellow lines show the lattice space of the crystalline Li. **d**, Schematic of the observed single-layer SEI structure on deposited Li in the 1 M LiFSI/DME-TFEO electrolyte.

to the oxidative decomposition of DME (Fig. 2a) and corrosion of the Al substrate by LiFSI, as shown in Supplementary Fig. 7c, where Al corrosion pits are observed on the cycled Al surface (at the back of the NMC811 electrode). In contrast, a significantly improved cycling performance was achieved using the 1 M LiFSI/DME-TFEO electrolyte, which has a capacity retention of 80% after 300 cycles and a high Coulombic efficiency of 99.7% over cycling. Al corrosion by LiFSI was also eliminated with the addition of TFEO solvent, as shown in Supplementary Fig. 7d. In addition, great cycling stability was obtained at both low (5 °C) and elevated temperature (55 °C), as shown in Supplementary Fig. 8.

Furthermore, the effects of charge and discharge rates on the cell performance of 1 M LiFSI/DME-TFEO in Li||NMC811 cells were evaluated and compared with those with the reference electrolyte. As shown in Fig. 2e, for the cell with the reference electrolyte, the specific capacities were almost identical at 200 mAh g^{-1} from charge rates C/5 to C/2, and were ~190 mAh g^{-1} at 1 C. However, when the charge rate was increased further to 2 C, a fast capacity decay was evident, and very limited specific capacity was obtained at 3 and 4 C charge rates. The cell capacity faded rapidly even when the rate was reduced back to C/5, which may have been caused by damage to the Li anode at high current density during the fast charge. In comparison, the cell with the 1 M LiFSI/DME-TFEO electrolyte performed significantly better at high charge rates, showing stable specific discharge capacities of ~175 mAh g^{-1} at 2 C, 160 mAh g^{-1} at 3 C and 137 mAh g^{-1} at 4 C. The specific capacity then recovered to 210 mAh g^{-1} after the charge rate was decreased back to C/5. For the cells with a constant charge rate of C/3 and different discharge rates, as shown in Fig. 2f, very slight differences in specific capacities were obtained at all of the discharge rates with the 1 M LiFSI/DME-TFEO electrolyte. Specific capacities of 182 and 178 mAh g^{-1} were shown at 3 and 4 C discharge rates, respectively, in the cell with the 1 M LiFSI/DME-TFEO electrolyte, while the cell with the reference electrolyte failed at the 3 C discharge rate. These results clearly show that the 1 M LiFSI/DME-TFEO electrolyte enables both fast charge and fast discharge processes in LMBs.

Postmortem analysis

The Li pulverization problem was largely minimized in an Li||NMC811 cell using the 1 M LiFSI/DME-TFEO electrolyte after long-term cycling. Figure 3a–c shows scanning electron microscopy (SEM) images with cross-sectional views of the three LMAs after 100 cycles. As shown in Fig. 3a,b, for the cells using the carbonate reference and 1 M LiFSI/DME electrolytes, the Li anodes were

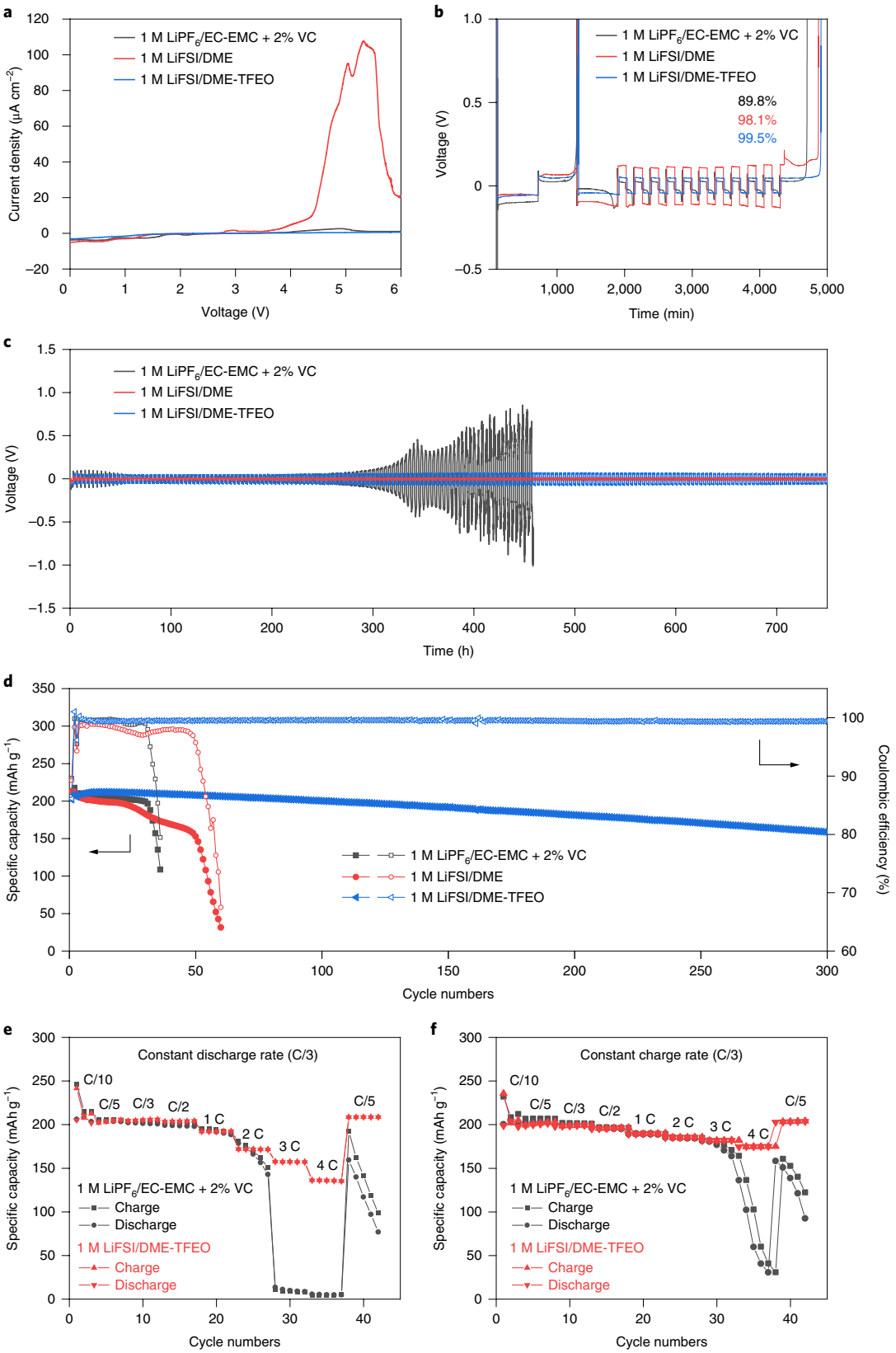

Fig. 2 | Electrochemical performances of different electrolytes. a–**d**, Electrochemical stability window (**a**), Li Coulombic efficiency (**b**), Li||Li cell cycling (**c**) and Li||NMC811 cell cycling performances (**d**) of the investigated electrolytes. In **d**, the lines with filled and open circles represent the specific capacity and Coulombic efficiency of the cells, respectively. **e**,**f**, Rate performance of Li||NMC811 cells at different charge C-rates with a constant discharge rate of C/3 (**e**) and a constant charge rate at C/3 with different discharge C-rates (**f**). Li||Li cycling was obtained at a current density of 0.5 mA cm^{-2} and an areal capacity of 1 mAh cm^{-2} for each plating or stripping step. Li||NMC811 cells consist of an NMC811 cathode (1.5 mAh cm^{-2}) and a thin Li foil (50 μm). They were charged and discharged between 2.8 and 4.4 V at a C/3 rate after two formation cycles at C/10, where 1 C = 1.5 mA cm^{-2}.

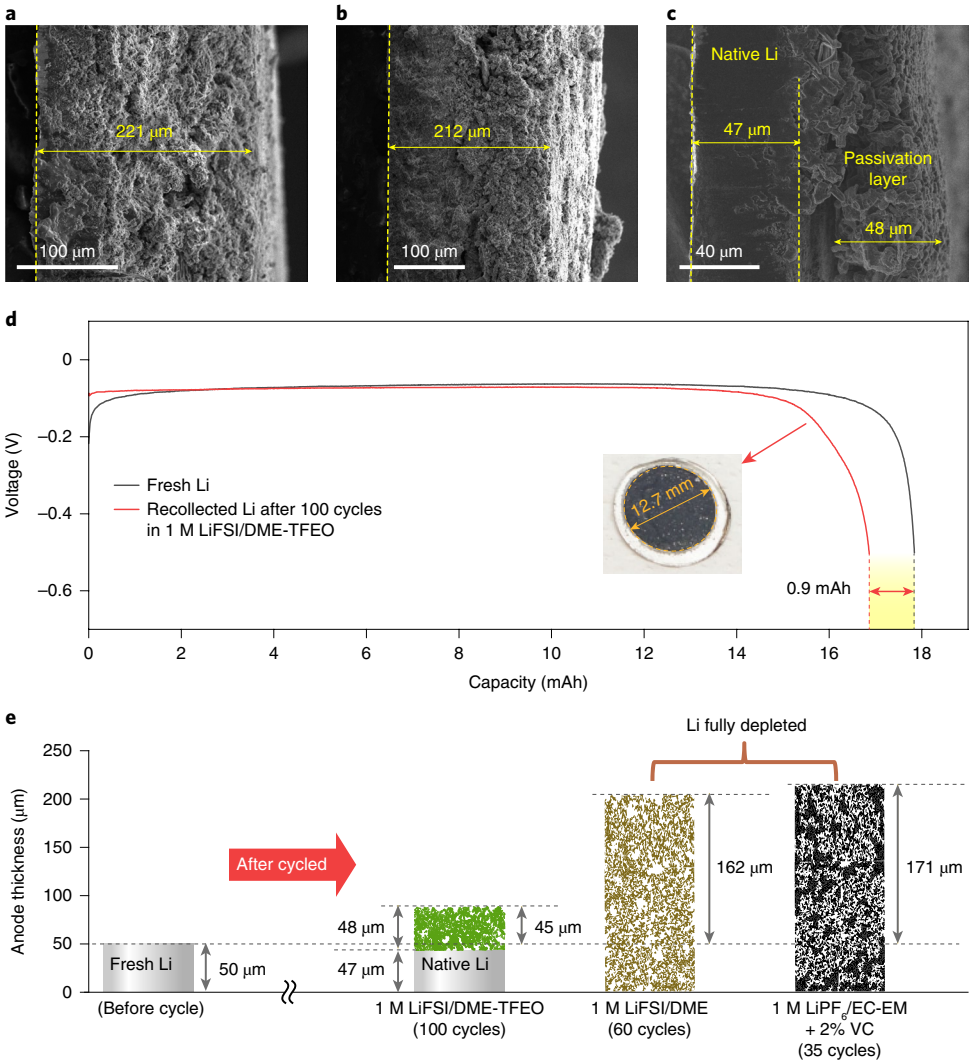

Fig. 3 | Li consumption and volumetric expansion after 100 cycles in Li||NMC811 cells. a–c, Cross-section views of SEM images of Li-metal electrodes cycled with electrolytes of 1 M $LiPF_6$/EC-EMC + 2% VC (**a**), 1 M LiFSI/DME (**b**) and 1 M LiFSI/DME-TFEO (**c**). **d**, Quantification of Li Loss during 100 cycles in 1 M LiFSI/DME-TFEO. Only 0.9 mAh of Li was lost in 100 cycles. Inset: optical photo of a cycled Li anode collected from the Li||NMC811 cell after 100 cycles in the 1 M LiFSI/DME-TFEO electrolyte. The diameter of the active Li anode was 12.7 mm—the same as that of the NMC811 cathode. **e**, Schematic of Li loss and corresponding thickness (volumetric) expansion after 100 cycles in Li||NMC811, while cells in 1 M $LiPF_6$/EC-EMC + 2% VC and 1 M LiFSI/DME failed sooner, at the 35th and 60th cycle, respectively, due to the complete depletion of Li.

completely consumed, and their thickness increased from 50 μm to 221 μm (that is, 171 μm expansion) and 212 μm (that is, 162 μm expansion), respectively. In contrast, ~47 μm fresh Li still remained after 100 cycles in the cell using the 1 M LiFSI/DME-TFEO electrolyte (Fig. 4c). The native metal lustre of the remaining Li layer can be distinguished easily from the dark passivation layer in the photo images, as shown in Supplementary Fig. 9. The thickness expansion was 45 μm, which is only around one-quarter of that of the Li metal cycled in the reference electrolyte. Supplementary Fig. 10d–f shows magnified versions of the SEM images shown in Supplementary Fig. 4a–c. Highly porous Li was generated on the Li anodes cycled in the reference and 1 M LiFSI/DME electrolytes. However, large granular structures were observed on the reacted Li side when using the 1 M LiFSI/DME-TFEO electrolyte. These were predominantly SEI shells accumulated over the 100 cycles. To determine the exact amount of Li loss, the cycled Li was collected from the Li||NMC811 cell after 100 cycles, then reassembled in an Li||Cu cell to strip the total active Li. As shown in Fig. 3d, the capacity of active Li after 100 cycles was 16.9 mAh. Compared with a fresh Li disk (identical (same weight) to the one used for cycling), having a capacity of 17.8 mAh, only 0.9 mAh (or 0.23 mg, based on the theoretical capacity of 3,860 mAh g^{-1}) of Li was lost in 100 cycles. The areal loss was 0.71 mAh cm^{-2} (0.18 mg cm^{-2}), as calculated by dividing the capacity difference by the reacted area (1.27 cm^2, facing the cathode). This value is equivalent to 3.37 μm Li, based on the density of Li (0.534 g cm^{-3}), which is in good agreement with the SEM imaging results shown in Fig. 3c. Figure 3e is a schematic of the Li depletion and thickness (volumetric) expansion of the Li anode after cycling of the original 50 μm fresh Li. The prevention of Li depletion/pulverization and greatly suppressed volumetric expansion of the Li anode in 1 M LiFSI/DME-TFEO is very promising for the practical application of the LMA in LMBs; it can not only enhance the cycling stability, but also make them much safer.

The significant improvement of the 1 M LiFSI/DME-TFEO electrolyte compared with the carbonate reference and 1 M LiFSI/DME electrolytes can be explained mainly by the different SEIs and CEIs generated in the different electrolytes. Figure 4a–i shows X-ray photoelectron spectroscopy (XPS) results for Li anodes retrieved after

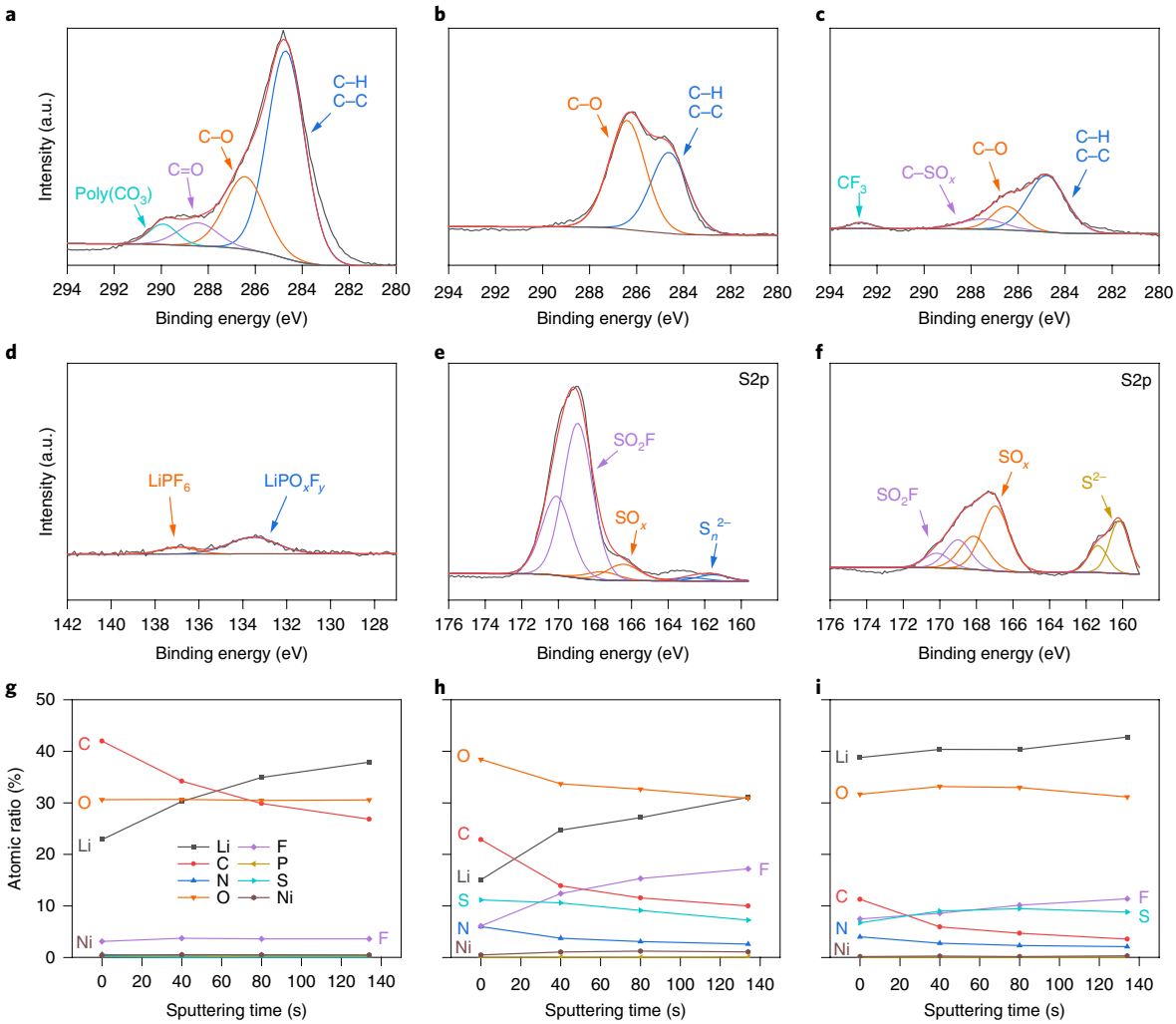

Fig. 4 | SEI information obtained by XPS measurement on Li electrodes after 100 cycles in Li||NMC811 cells with electrolytes. a–i, C 1*s* spectra (**a**–**c**), P 2*p* spectra (**d**) and S 2*p* surface spectra (**e** and **f**), as well as quantified atomic composition ratios of the SEI at different sputtering times (**g**–**i**), for 1 M $LiPF_6$/EC-EMC + 2% VC (**a**, **d** and **g**), 1 M LiFSI/DME (**b**, **e** and **h**) and 1 M LiFSI/DME-TFEO (**c**, **f** and **l**). All of the XPS results were fitted with CasaXPS software. The binding energy was calibrated with C 1*s* at 284.8 eV. For fitting, Shirley BG type was used for background subtraction and GL(30) line shape was used for peak fit.

100 cycles. The C 1*s* spectrum was selected as a representative of organic species; it usually contains C–H/C–C, C–O and polycarbonates that are mainly derived from electrolyte solvents. As shown in Fig. 4a–c, the Li electrode cycled in the reference electrolyte (Fig. 5a) had the highest C 1*s* intensity, while the Li cycled in 1 M LiFSI/DME showed less C 1*s* intensity, and the Li anode cycled in 1 M LiFSI/DME-TFEO showed the lowest C 1*s* intensity. These results clearly indicate that there was less solvent decomposition on the Li-metal surface in the 1 M LiFSI/DME-TFEO electrolyte.

The P 2*p* and S 2*p* spectra typically represent the contributions from inorganic components generated in the SEI, which are derived from the conductive salts ($LiPF_6$ or LiFSI). The S 2*p* intensities for Li cycled in 1 M LiFSI/DME and 1 M LiFSI/DME-TFEO were much higher than the P 2*p* intensity obtained for Li cycled in the reference electrolyte. This result indicates that LiFSI was preferentially decomposed, and participated in SEI formation. The difference between these two electrolytes is in the decomposition products in the SEI. Apparent SO_2F and a small S_n^{2-} signal were observed for the 1 M LiFSI/DME electrolyte, while larger SO_x and S^{2-} signals are shown for the 1 M LiFSI/DME-TFEO electrolyte, meaning that LiFSI is more completely reduced with the addition of TFEO. Together with the C 1*s* spectra, it can be concluded that LiFSI, rather than solvent (either carbonate or ether), is preferentially decomposed in the 1 M LiFSI/DME-TFEO electrolyte to form SEI on the Li surface, which is consistent with the results observed with cryo-EM. In addition, the peak at 292.5 eV, attributed to the CF_3 group (Fig. 4c), indicates that TFEO participates in SEI formation simultaneously with LiFSI decomposition.

In addition to the surface analysis, more detailed information was obtained with an XPS depth profile with argon sputtering. Figure 4g–i shows the atomic ratios of selected elements on the cycled Li anodes collected at different depths. Detailed and fitted XPS spectra for different electrolytes are shown in Supplementary Figs. 11–13. As shown in Fig. 4g for the Li anode cycled in the reference electrolyte, more organic species containing C were observed on the surface of the SEI. With the depth profiling (from the surface to the bottom (close to the Li metal)), the organic species (C as an indicator) derived from the solvent significantly decreased while the inorganic species (Li as an indicator) increased. The same trend was found in 1 M LiFSI/DME. This trend is well known as 'two-sublayer SEI' in the literature, where the inner layer is rich in inorganic species and the outer layer is rich in organic species[18,20].

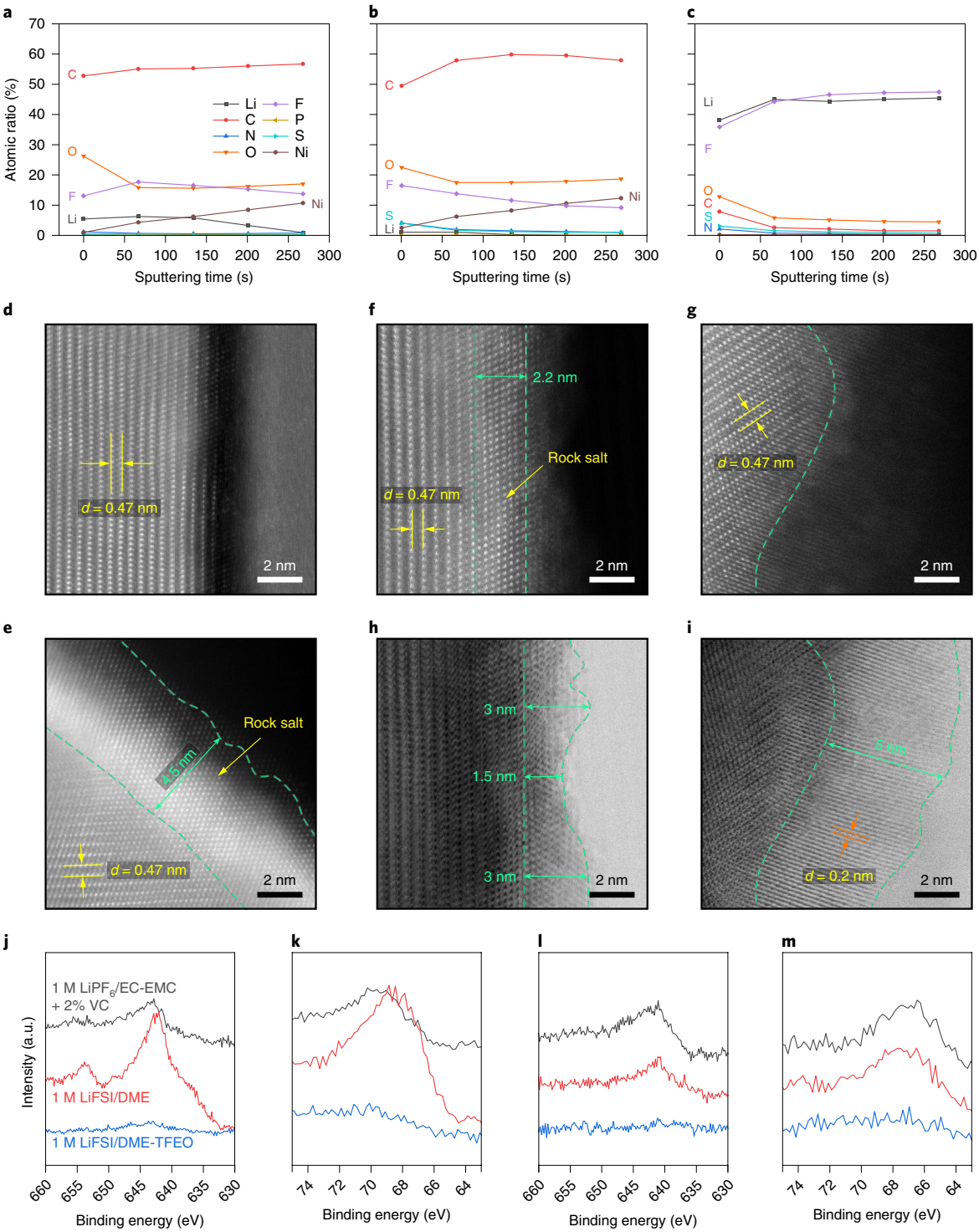

Fig. 5 | Structural and CEI/SEI properties of the electrodes. a–c, Quantified atomic composition ratios of the CEI obtained by XPS spectra for the NMC811 electrodes collected from cells with 1 M $LiPF_6$/EC-EMC + 2% VC (**a**), 1 M LiFSI/DME (**b**) and 1 M LiFSI/DME-TFEO (**c**) after 100 cycles. **d–i**, HAADF-STEM (**d–g**) and ABF-STEM images (**h** and **i**) of pristine (**d**) and cycled NMC811 electrodes collected from cells with 1 M $LiPF_6$/EC-EMC + 2% VC (**e**), 1 M LiFSI/DME (**f** and **h**) and 1 M LiFSI/DME-TFEO (**g** and **i**) after 100 cycles. *d* represents the spacing between adjacent lattice planes. **j–m**, Mn 2*p* (**j** and **l**) and Ni 3*p* XPS spectra (**k** and **m**) of the NMC811 cathodes (**j** and **k**) and Li anodes (**l** and **m**) after 100 cycles in Li||NMC811 cells.

In strong contrast, the atomic ratio of different elements was almost constant from the surface to the bottom of the SEI layer formed in the 1 M LiFSI/DME-TFEO electrolyte, indicating homogeneous element distribution in this SEI at different depths. This is the first time an SEI layer with essentially the same composition from the surface to the bottom has been reported, which is beyond the known mosaic and multilayer SEIs[18]. Together with the uniformity in the horizontal coverage of the SEI on the Li surface observed with cryo-EM (Fig. 1), this SEI layer is uniform along all three dimensions. Its unique properties greatly suppressed the Li–electrolyte

interactions, minimized Li and electrolyte depletion, and enabled enhanced cycling performance with minimal Li pulverization.

In addition to stabilizing the Li anode and minimizing pulverization of Li during cycling, 1 M LiFSI/DME-TFEO also greatly stabilized the NMC811 cathode. Figure 5a–c shows the atomic ratio of the CEI layer formed on the surface of the NMC811 cathode in different electrolytes. An LiF-rich CEI (as indicated by the high Li and F ratios shown in Fig. 5c) was formed on the surface of NMC811 in the TFEO-based electrolyte, while organic-rich CEIs (high C ratio (Fig. 5a,b)) were obtained in the reference carbonate and 1 M LiFSI/DME electrolytes. Detailed and fitted XPS spectra for different electrolytes are shown in Supplementary Figs. 14–16. Figure 5d–i shows the high-angle annular dark-field scanning transmission electron microscopy (TEM) (HAADF-STEM) and annular bright-field scanning TEM (ABF-STEM) imaging results of the fresh and cycled NMC811 electrodes. A layered structure was clearly observed in the pristine NMC811 electrode (Fig. 5d). For the electrode cycled in carbonate electrolyte, the surface underwent a severe phase transition, with an accumulation of ~4.5 nm of disordered rock salt phase on the cathode surface (Fig. 5e), which was caused by the electrolyte–NMC811 interactions. The surface lattice layers of NMC811 electrode were subject to a certain degree of intermixing, where the Li sites were partially occupied by the anti-site Ni ions[45]. This reconstruction also existed in the NMC811 electrode cycled in 1 M LiFSI/DME, with a rock salt thickness of 2.2 nm (Fig. 5f). In contrast, for the same cycling condition in 1 M LiFSI/DME-TFEO, the electrode surface maintained a layered structure (Fig. 5g) that was comparable to the pristine sample (Fig. 5d), indicating that the detrimental phase transition was effectively suppressed in this electrolyte. The origin of these beneficial effects can be attributed to the formation of a uniform LiF-rich CEI layer (~5 nm), as outlined by the green dashed lines in Fig. 5i of the corresponding ABF-STEM image, which has been widely recognized as providing the sustained protection for battery operation[46], while the uneven and organic-rich CEI (Fig. 5h) formed in 1 M LiFSI/DME electrolyte is less protective. XPS results of the Mn 2*p* (Fig. 5j) and Ni 3*p* (Fig. 5k) of the NMC811 electrodes also confirmed that no Mn or Ni was detected on the surface of the NMC811 cycled in the 1 M LiFSI/DME-TFEO electrolyte, because of the dense and continuous LiF layer formed on its surface, while Mn and Ni were found on the surface of both NMC811 electrodes cycled in either reference electrolyte or 1 M LiFSI/DME electrolyte. The Mn and Ni content in the surface of NMC811 electrodes tends to dissolve, cross over and deposit on the Li anode[47], as shown in the Mn 2*p* (Fig. 5l) and Ni 3*p* spectra (Fig. 5m) of the cycled Li anodes, where Mn and Ni were found on the Li anodes cycled in reference electrolyte and 1 M LiFSI/DME electrolyte. However, due the effective protection of the LiF layer on the NMC811 cathode cycled in the 1 M LiFSI/DME-TFEO electrolyte, the amount of transition metals dissolved into the electrolyte and crossed over to deposit on the Li anode was significantly reduced. Stabilization of both the NMC811 cathode and the Li anode is required for the long-term cycling stability of Li||NMC811 cells.

Conclusion

We propose that a class of fluorinated orthoformate solvents is used in electrolytes for LMBs. A TFEO-based electrolyte such as 1 M LiFSI/DME-TFEO (1:9 by weight; 1.2:3 by mole) forms a highly homogeneous, amorphous and monolithic SEI layer on an LMA, rather than the mosaic- or multilayer-type SEI structure reported previously. This SEI layer is rich in inorganic species and leads to high Coulombic efficiency for LMAs without Li dendrite growth. Together with a crystalline, LiF-rich CEI formed on the NMC811 cathode, this electrolyte enables long-term cycling stability of Li||NMC811 cells with minimal pulverization of LMA, which is one of the main barriers to the practical application of LMBs. In addition, it allows fast charging and discharging of Li||NMC811 cells at rates of up to 4 C (~6 mA cm^{-2}). All of these results show that the newly developed TFEO-based electrolyte is very promising for practical applications in high-voltage LMBs.

Methods

Materials. Battery-grade $LiPF_6$, EC, EMC, VC and DME were used as received from BASF Battery Materials. TFEO was purchased from SynQuest Laboratories and dried with 4 Å molecular sieves (Sigma–Aldrich) until the moisture content was <20 ppm when titrated by the Karl–Fischer method. LiFSI (99%) was provided free of charge by Nippon Shokubai and pre-dried at 120 °C overnight before use. The NMC811 material was purchased from Targray.

Density functional theory (DFT) calculation. DFT calculations of the HOMO and lowest unoccupied molecular orbital (based on geometry optimization and frequency computation) were performed with the GAUSSIAN 09 software package with a basis set of 6-311++G(d,p)[27,48,49].

Electrolyte and electrode preparation. The electrolytes were prepared by dissolving the conductive salt $LiPF_6$ or LiFSI in the selected solvent (mixture) and additive inside an MBraun glovebox filled with purified argon, where the moisture and oxygen content was <1 ppm. Specifically, 1 M $LiPF_6$/EC-EMC (1:1 by weight) + 2% VC, 1 M LiFSI/DME and 1 M LiFSI/DME-TFEO (1:9 by weight and 1.2:3 by mole) were used. In the TFEO-based electrolyte, we chose a low DME:high TFEO weight ratio because TFEO has very poor solubility with LiFSI. To keep the salt concentration of 1 M in the conventional electrolytes, DME was used to dissolve the LiFSI. A weight ratio of 1:9 for DME and TFEO was the minimum amount of DME to obtain the desired 1 M LiFSI-based electrolyte and the maximum amount of TFEO for good electrolyte anodic stability. The NMC811 cathodes were prepared by slurry coating on Al foil, comprising 96 wt% NMC811, 2 wt% Super C65 (as conductive carbon) and 2 wt% polyvinylidene difluotide (as binder). The areal capacity loading was about 1.5 mAh cm^{-2}, and the cathode was punched into 1.27 cm^2 disks and further dried at 120 °C overnight. Li on Cu foil (50 ± 2 µm), received from China Energy Lithium, was used as received.

Electrochemical tests. Electrochemical stability windows were measured separately for anodic stability and cathodic stability by linear sweeping voltammetry from open circuit potential to 6 and 0 V, respectively, with a scan rate of 0.1 mV s^{-1} on a CHI660C electrochemical workstation. CR2032 coin cells were assembled for this measurement, in which a piece of Al foil (for anodic sweeping) or Cu foil (for cathodic sweeping) was used as a cathode, a piece of separator (polyethylene; Asahi Hipore) and an Li chip (250 µm thick; 1.50 cm diameter; MTI) were sandwiched together, and 75 µl electrolyte was added to each cell before it was crimped inside the argon-filled glovebox. The Li Coulombic efficiency was measured in the same setup of Li||Cu configuration as was used for the cathodic stability tests, using the Coulombic efficiency protocol (method 3 with a total charge (Q_T) = 5 mAh cm^{-2} and a cycled charge (Q_C) = 1 mAh cm^{-2} and n = 10) reported in our previous work[50]. Li (1 mAh cm^{-2}) was deposited on Cu at a current of 0.5 mA cm^{-2} and collected for Li deposition morphology measurement. The Li||Li or Li||NMC811 cells were also assembled in the same way by replacing Al foil with an Li chip or NMC811 electrode. For the Li||NMC811 cell, 50-µm-thick Li on Cu foil was used as the LMA. The cycling performance of Li||Li cells was evaluated by plating/stripping 1 mAh cm^{-2} of Li at a current density of 0.5 mA cm^{-2}. The Li||NMC811 cells were tested within a voltage range of 2.8–4.4 V at C/3 charge and discharge rates after two formation cycles at C/10, where 1 C was 200 mA g^{-1} (~1.5 mA cm^{-2}). The rate performance was tested in two modes, by fixing either a constant charge rate of C/3 or a discharge rate of C/3 and varying the discharge or charge rates, respectively, from C/5 to C/3, C/2, 1C, 2C, 3C, 4C and C/5 for five cycles each.

Characterizations. For postmortem analyses, including SEM, XPS and TEM measurements, cycled coin cells were disassembled inside the glovebox to collect the Cu substrates, Li foils or NMC cathodes. These electrodes were rinsed with dimethyl carbonate or DME solvent to remove residual electrolytes, dried, and then sealed in airtight containers in the glovebox before being transferred for further characterizations. SEM measurements were carried out on a Helios focused-ion-beam scanning electron microscope at an accelerating voltage of 5 kV and a current of 86 pA. XPS measurements were performed with a Physical Electronics Quantera scanning X-ray microprobe. A focused monochromatic Al Kα X-ray (1,486.7 eV) source was used for excitation, and a spherical section analyzer and a pass energy of 69.0 eV were used for high-energy-resolution spectra collection. The sample sputtering parameters of Ar^+ ions (2 kV; 2 µA; 45° incident angle) were used for the depth profiling investigation. The sputtering time increments for the Li-metal samples were 0, 40, 80 and 134 s. The sputtering time increments for the NMC samples were 0, 67, 134, 201 and 268 s. The TEM samples were prepared using the FEI Helios Dual Beam system. A secondary particle of NMC811 was selected randomly for the lift-out processes. A Pt layer of ~2 µm was coated on the targeted particle, which was then extracted along with the capping layers and welded to the TEM grid[45]. The thinning processes were performed at 30 kV, followed by 5 and then 2 kV to polish the surface and remove the damaged layers[45]. The as-prepared

sample was characterized using a JEOL JEM-ARM200CF spherical-aberration-corrected microscope[45]. The convergence angle was set at 20.6 mrad for imaging, and the signals at 90–370 and 10–23 mrad were collected for HAADF-STEM and STEM-ABF imaging, respectively. The Li sample for cryo-EM was prepared by depositing Li on the TEM grid, at a current of 2 mA and a capacity of 0.2 mAh, with 1 M LiFSI/DME-TFEO. The sample was then dabbed with DME and frozen, to carry out the cryo-EM according to the procedures reported by Li et al.[19].

Data availability

The data that support the plots within this paper and other findings of this study are available from the corresponding author upon reasonable request.

Received: 23 March 2019; Accepted: 8 August 2019;
Published online: 13 September 2019

References

1. Whittingham, M. S. Ultimate limits to intercalation reactions for lithium batteries. *Chem. Rev.* **114**, 11414–11443 (2014).
2. Zhang, J.-G., Xu, W. & Henderson, W. A. *Lithium Metal Anode and Rechargeable Li Metal Batteries* (Springer International Publishing, 2017).
3. Liu, J. et al. Pathways for practical high-energy long-cycling lithium metal batteries. *Nat. Energy* **4**, 180–186 (2019).
4. Lin, D., Liu, Y. & Cui, Y. Reviving the lithium metal anode for high-energy batteries. *Nat. Nanotechnol.* **12**, 194–206 (2017).
5. Wang, J. et al. Superconcentrated electrolytes for a high-voltage lithium-ion battery. *Nat. Commun.* **7**, 12032 (2016).
6. Erickson, E. M. et al. Review—development of advanced rechargeable batteries: a continuous challenge in the choice of suitable electrolyte solutions. *J. Electrochem. Soc.* **162**, A2424–A2438 (2015).
7. Cheng, X.-B., Zhang, R., Zhao, C.-Z. & Zhang, Q. Toward safe lithium metal anode in rechargeable batteries: a review. *Chem. Rev.* **117**, 10403–10473 (2017).
8. Ding, M. S., von Cresce, A. & Xu, K. Conductivity, viscosity, and their correlation of a super-concentrated aqueous electrolyte. *J. Phys. Chem. C.* **121**, 2149–2153 (2017).
9. Liu, B., Zhang, J.-G. & Xu, W. Advancing lithium metal batteries. *Joule* **2**, 833–845 (2018).
10. Pang, Q. et al. Tuning the electrolyte network structure to invoke quasi-solid state sulfur conversion and suppress lithium dendrite formation in Li–S batteries. *Nat. Energy* **3**, 783–791 (2018).
11. Chen, S. et al. High-efficiency lithium metal batteries with fire-retardant electrolytes. *Joule* **2**, 1548–1558 (2018).
12. Ren, X. et al. Localized high-concentration sulfone electrolytes for high-efficiency lithium-metal batteries. *Chem* **4**, 1877–1892 (2018).
13. Li, N.-W. et al. A flexible solid electrolyte interphase layer for long-life lithium metal anodes. *Angew. Chem. Int. Ed.* **57**, 1505–1509 (2018).
14. Fan, X. et al. Non-flammable electrolyte enables Li-metal batteries with aggressive cathode chemistries. *Nat. Nanotechnol.* **13**, 715–722 (2018).
15. Zeng, Z. et al. Non-flammable electrolytes with high salt-to-solvent ratios for Li-ion and Li-metal batteries. *Nat. Energy* **3**, 674–681 (2018).
16. Jiao, S. H. et al. Stable cycling of high-voltage lithium metal batteries in ether electrolytes. *Nat. Energy* **3**, 739–746 (2018).
17. Aurbach, D., Zinigrad, E., Cohen, Y. & Teller, H. A short review of failure mechanisms of lithium metal and lithiated graphite anodes in liquid electrolyte solutions. *Solid State Ion.* **148**, 405–416 (2002).
18. Peled, E. & Menkin, S. Review—SEI: past, present and future. *J. Electrochem. Soc.* **164**, A1703–A1719 (2017).
19. Li, Y. et al. Atomic structure of sensitive battery materials and interfaces revealed by cryo–electron microscopy. *Science* **358**, 506–510 (2017).
20. Xu, K. Electrolytes and interphases in li-ion batteries and beyond. *Chem. Rev.* **114**, 11503–11618 (2014).
21. Wang, X. et al. New insights on the structure of electrochemically deposited lithium metal and its solid electrolyte interphases via cryogenic TEM. *Nano Lett.* **17**, 7606–7612 (2017).
22. Noh, H.-J., Youn, S., Yoon, C. S. & Sun, Y.-K. Comparison of the structural and electrochemical properties of layered $Li[Ni_xCo_yMn_z]O_2$ ($x=1/3$, 0.5, 0.6, 0.7, 0.8 and 0.85) cathode material for lithium-ion batteries. *J. Power Sources* **233**, 121–130 (2013).
23. Yan, G. et al. Fluorinated solvents for high-voltage electrolyte in lithium-ion battery. *J. Solid State Electrochem.* **21**, 1589–1597 (2017).
24. Xu, K. Nonaqueous liquid electrolytes for lithium-based rechargeable batteries. *Chem. Rev.* **104**, 4303–4418 (2004).
25. Cao, X. et al. High voltage $LiNi_{0.5}Mn_{1.5}O_4/Li_4Ti_5O_{12}$ lithium ion cells at elevated temperatures: carbonate- versus ionic liquid-based electrolytes. *ACS Appl. Mater. Interfaces* **8**, 25971–25978 (2016).
26. Park, M. S. et al. A highly reversible lithium metal anode. *Sci. Rep.* **4**, 3815 (2014).
27. Zhang, Z. et al. Fluorinated electrolytes for 5 V lithium-ion battery chemistry. *Energy Environ. Sci.* **6**, 1806–1810 (2013).
28. Fan, X. et al. Highly fluorinated interphases enable high-voltage Li-metal batteries. *Chem* **4**, 174–185 (2018).
29. Noguchi, T., Hasegawa, T., Yamauchi, H., Yamazaki, I. & Utsugi, K. Effect of using fluorinated ether and sulfone as electrolyte solvents for lithium ion batteries with lithium-rich layered cathodes and silicon oxide anodes. *ECS Trans.* **80**, 291–303 (2017).
30. Suo, L. et al. Fluorine-donating electrolytes enable highly reversible 5-V-class Li metal batteries. *Proc. Natl Acad. Sci. USA* **115**, 1156–1161 (2018).
31. Böttcher, T. et al. in *Advanced Fluoride-Based Materials for Energy Conversion* (eds Nakajima, T. & Groult, H.) 125–145 (Elsevier, 2015).
32. Moon, H. et al. Solvent activity in electrolyte solutions controls electrochemical reactions in Li-ion and Li-sulfur batteries. *J. Phys. Chem. C* **119**, 3957–3970 (2015).
33. Yu, L. et al. A localized high-concentration electrolyte with optimized solvents and lithium difluoro(oxalate)borate additive for stable lithium metal batteries. *ACS Energy Lett.* **3**, 2059–2067 (2018).
34. Zheng, J. et al. Extremely stable sodium metal batteries enabled by localized high-concentration electrolytes. *ACS Energy Lett.* **3**, 315–321 (2018).
35. Doi, T., Shimizu, Y., Hashinokuchi, M. & Inaba, M. Dilution of highly concentrated $LiBF_4$/propylene carbonate electrolyte solution with fluoroalkyl ethers for 5-V $LiNi_{0.5}Mn_{1.5}O_4$ positive electrodes. *J. Electrochem. Soc.* **164**, A6412–A6416 (2017).
36. Chen, S. et al. High-voltage lithium-metal batteries enabled by localized high-concentration electrolytes. *Adv. Mater.* **30**, 1706102 (2018).
37. Yamada, Y. & Yamada, A. Review—superconcentrated electrolytes for lithium batteries. *J. Electrochem. Soc.* **162**, A2406–A2423 (2015).
38. Yamada, Y. et al. Unusual stability of acetonitrile-based superconcentrated electrolytes for fast-charging lithium-ion batteries. *J. Am. Chem. Soc.* **136**, 5039–5046 (2014).
39. Qian, J. et al. High rate and stable cycling of lithium metal anode. *Nat. Commun.* **6**, 6362 (2015).
40. Ren, X. et al. Enabling high-voltage lithium metal batteries under practical conditions. *Joule* **3**, 1662–1676 (2019).
41. Von Cresce, A. & Xu, K. Electrolyte additive in support of 5 V Li ion chemistry. *J. Electrochem. Soc.* **158**, A337–A342 (2011).
42. Tan, S. et al. Tris(hexafluoro-iso-propyl)phosphate as an SEI-forming additive on improving the electrochemical performance of the $Li[Li_{0.2}Mn_{0.56}Ni_{0.16}Co_{0.08}]O_2$ cathode material. *J. Electrochem. Soc.* **160**, A285–A292 (2013).
43. Von Aspern, N. et al. Phosphorus additives for improving high voltage stability and safety of lithium ion batteries. *J. Fluor. Chem.* **198**, 24–33 (2017).
44. Ren, X. et al. Localized high-concentration sulfone electrolytes for high-efficiency lithium-metal batteries. *Chem* **4**, 1877–1892 (2018).
45. Zou, L. et al. Solid–liquid interfacial reaction trigged propagation of phase transition from surface into bulk lattice of Ni-rich layered cathode. *Chem. Mater.* **30**, 7016–7026 (2018).
46. Wang, C., Meng, Y. S. & Xu, K. Perspective—fluorinating interphases. *J. Electrochem. Soc.* **166**, A5184–A5186 (2019).
47. Evertz, M. et al. Unraveling transition metal dissolution of $Li_{1.04}Ni_{1/3}Co_{1/3}Mn_{1/3}O_2$ (NCM 111) in lithium ion full cells by using the total reflection X-ray fluorescence technique. *J. Power Sources* **329**, 364–371 (2016).
48. Cao, X. et al. Ester modified pyrrolidinium based ionic liquids as electrolyte component candidates in rechargeable lithium batteries. *Z. Anorg. Allg. Chem.* **641**, 2536–2542 (2015).
49. Zhan, C.-G., Nichols, J. A. & Dixon, D. A. Ionization potential, electron affinity, electronegativity, hardness, and electron excitation energy: molecular properties from density functional theory orbital energies. *J. Phys. Chem. A* **107**, 4184–4195 (2003).
50. Adams, B. D., Zheng, J., Ren, X., Xu, W. & Zhang, J.-G. Accurate determination of coulombic efficiency for lithium metal anodes and lithium metal batteries. *Adv. Energy Mater.* **8**, 1702097 (2018).

Acknowledgements

This work has been supported by the Assistant Secretary for Energy Efficiency and Renewable Energy, Vehicle Technologies Office, of the US Department of Energy (DOE), through the Advanced Battery Materials Research program (Battery500 Consortium) under contract number DE-AC02-05CH11231. The SEM, TEM and XPS were conducted in the William R. Wiley Environmental Molecular Sciences Laboratory—a national scientific user facility sponsored by the DOE's Office of Biological and Environmental Research and located at the Pacific Northwest National Laboratory. The Pacific Northwest National Laboratory is operated by Battelle for the DOE under the contract DE-AC05-76RL01830. The LiFSI salt was provided by K. Murata of Nippon Shokubai.

Author contributions

J.-G.Z., W.X. and X.C. proposed the research and designed the experiments. X.C. performed the electrochemical measurements and conducted the SEM

observations, with help from X.R. L.Z., B.E.M., B.W.A. and C.W. performed the focused-ion-beam SEM and TEM. M.H.E. performed the XPS measurements. H.W., W.H. and Y.C. carried out the cryo-EM. C.N. and H.L. prepared the NMC811 electrodes. X.C., W.X. and J.-G.Z. prepared the manuscript, with input from all other co-authors.

Competing interests

The authors declare no competing interests.

Additional information

Supplementary information is available for this paper at https://doi.org/10.1038/s41560-019-0464-5.

Reprints and permissions information is available at www.nature.com/reprints.

Correspondence and requests for materials should be addressed to W.X. or J.-G.Z.

Publisher's note Springer Nature remains neutral with regard to jurisdictional claims in published maps and institutional affiliations.

© The Author(s), under exclusive licence to Springer Nature Limited 2019